

Article

Fabrication of Ni-Based Bimodal Porous Catalyst for Dry Reforming of Methane

Linghui Lyu ^{1,†}, Yunxing Han ^{1,†}, Qingxiang Ma ^{1,*}, Shengene Makpal ¹, Jian Sun ^{1,2,*} , Xinhua Gao ¹, Jianli Zhang ¹, Hui Fan ¹ and Tian-Sheng Zhao ¹

¹ State Key Laboratory of High-efficiency Coal Utilization and Green Chemical Engineering, College of Chemistry and Chemical Engineering, Ningxia University, Yinchuan 750021, China; lyulinghui@163.com (L.L.); hanyunxing802@163.com (Y.H.); Sh.Makpal@gmail.com (S.M.); gXH@nxu.edu.cn (X.G.); zhangjl@nxu.edu.cn (J.Z.); fanhui@nxu.edu.cn (H.F.); zhaots@nxu.edu.cn (T.-S.Z.)

² Dalian National Laboratory for Clean Energy (DNL), Dalian Institute of Chemical Physics, Chinese Academy of Sciences, Dalian 116023, China

* Correspondence: maqx@nxu.edu.cn (Q.M.); sunj@dicp.ac.cn (J.S.); Tel.: +86-0951-206-2393 (Q.M.); +86-0411-8437-9283 (J.S.)

† These authors contribute equally.

Received: 19 August 2020; Accepted: 13 October 2020; Published: 20 October 2020



Abstract: Dry reforming of methane (DRM) can effectively convert two greenhouse gases into high-valued chemicals, in which the syngas produced by the reaction can be directly used as raw gases for Fischer–Tropsch synthesis and methanol synthesis. Ni-based catalysts for the DRM reaction with comparable initial activity to noble metals are the focus of most researchers, but their poor carbon deposition resistance easily causes their low stability. More importantly, the nickel loading will affect the catalytic activity and carbon deposition resistance of the catalyst. Herein, a series of Ni/Al₂O₃ catalysts with bimodal pores was prepared and characterized by X-ray diffraction (XRD), N₂ physical adsorption–desorption, H₂-temperature programmed reduction (H₂-TPR), temperature programmed hydrogenation (TPH), Raman, and thermogravimetric analysis (TG). The results show that the interesting bimodal structure catalysts could provide a high surface area and contribute to the mass transfer. Besides, the catalytic performance of the DRM reaction is sensitive to nickel loadings. In this study, the Ni/Al₂O₃ catalyst with nickel loadings of 6% and 8% exhibited excellent catalytic activity and carbon deposition resistance. These findings will provide a new strategy to design a highly efficient and stable heterogeneous catalyst for industry.

Keywords: dry reforming of methane; bimodal porous nickel-based catalysts; nickel loading; carbon deposition

1. Introduction

CH₄ is the main component of natural gas. It is also a greenhouse gas with a greenhouse effect 20 times that of CO₂ [1]. The chemical conversion of CH₄ is divided into direct and indirect conversions. The direct conversion of methane has great advantages in theory, however, the high chemical stability of CH₄ makes it difficult to achieve industrialization by direct conversion. The indirect conversion of CH₄ is to convert it into synthetic gas, one of the most important substrates to produce other chemical products such as olefin and dimethyl ether in the chemical industry [2–4].

CH₄ reforming to syngas is commonly found in three ways: steam reforming of methane (SRM), partial oxidation of methane (POM), and dry reforming of methane (DRM). The advantages of DRM over other reforming make it very attractive. This reaction effectively utilizes two greenhouse gases to achieve carbon recycling, and it also generates a favorable H₂/CO ratio for Fischer–Tropsch synthesis,

methanol synthesis, and the like; furthermore, it can be used as an energy storage medium for energy transfer [5–9]. Currently, there are still some problems in the dry reforming of methane, especially the severe carbon deposition of catalysts, which greatly limits the industrial development of the reaction.

The catalysts of DRM can be divided into noble metal catalysts with Pt [10], Pd [11], Rh [12], Ru [13], Ir [14], and the like as active centers, and transition metal catalysts with Ni, Co, Fe, etc. as active centers [15]. Though noble metals are less sensitive to carbon deposition, non-noble metals have attracted the attention of researchers because of the big difference in price. Studies have shown that the catalytic activity sequence of non-noble metal catalysts is $\text{Ni} > \text{Co} > \text{Fe}$. Therefore, most researchers focus on Ni-based catalysts [16–18]. Hou et al. [19] also compared the catalytic activity of noble metal catalysts with non-noble metal catalysts. Studies have shown that Ni-based catalysts have comparable initial activities to noble metals, but their poor carbon deposition resistance makes it easy to form carbon deposits on the catalyst surface. This causes the reaction tube pressure to rise and the catalytic activity to decrease. The carbon deposit not only covers the active metal, which means that it does not make contact with the reactant molecules, but also blocks the pores of the catalyst and increases the diffusion resistance of reactants and product molecules. The problem of carbon deposition has become the “bottleneck” for the industrialization of the dry reforming of methane [20–22].

Many efforts have been made to reduce the carbon deposition on the nickel particles. It has been reported that a trimetallic $\text{Co}_x\text{Ni}_y\text{Mg}_{100-x-y}\text{O}$ catalyst [23] has great carbon resistance for the Co-rich Co-Ni alloy, accelerating the gasification of coke intermediates. Zhou and his co-workers [24] used a single-source precursor to generate a Ru-Ni-MgO catalyst and the Ni-rich Ru-Ni alloy was identified as a carbon-resistant catalyst in $\text{CH}_4\text{-CO}_2$ reforming, for Ru, slowing down the carbon deposition rate via elevating the methane dissociation barrier. Mohcin Akri et al. [25] reported that atomically dispersed Ni single atoms, stabilized by interaction with Ce-doped hydroxyapatite, only activating the first C-H bond in CH_4 , thus avoiding methane deep decomposition into carbon, were highly active and coke-resistant catalytic sites for the DRM reaction. Wang and Ruckenstein [26] studied the effect of reduced supports (CeO_2 , Nb_2O_5 , Ta_2O_5 , TiO_2 , and ZrO_2) and irreducible metal oxides ($\gamma\text{-Al}_2\text{O}_3$, La_2O_3 , MgO , SiO_2 , and Y_2O_3) used as supports on Rh catalysts. In summary, MgO and $\gamma\text{-Al}_2\text{O}_3$ are the most promising supports.

The nickel loading can affect the catalytic activity and carbon deposition resistance of the catalysts. Sepelchik et al. [27] compared the catalysts with different nickel loadings for the DRM reaction at 700 °C, finding that the catalytic activity of the catalysts increases with the increase in the nickel loading. However, as the nickel content is too high, the Ni particles are easily migrated and sintered at a high temperature that leads to form a large amount of carbon deposits.

Ni-based catalysts are easily deactivated at high temperature due to carbon deposition. To solve this problem, a bimodal porous structure catalyst was designed, which had the advantages of two types of porous structure. The mesoporous structure provides a large specific surface area, which is beneficial to improve the dispersion of Ni; the macroporous structure provides a channel for the diffusion of reactants and product molecules, which facilitates the rapid diffusion of gas molecules in the pores.

In this paper, based on bimodal porous nickel-based catalysts, the optimal Ni loading was selected by investigating the effect of nickel loading on the catalytic performance and carbon deposition resistance of the catalysts. The relationship between properties of bimodal series catalysts and the catalytic performance is demonstrated in detail in the following parts.

2. Results and Discussion

2.1. Fresh Catalysts Characterization

Figure 1a presents the N_2 adsorption–desorption isotherm diagram for different nickel loadings catalysts. It is clearly seen that all catalysts exhibit a typical type IV adsorption isotherm, and the distinct H_1 -type hysteresis loop between $P/P_0 = 0.4$ and 0.9 indicates the existence of a mesoporous structure. The isotherms of all bimodal porous catalysts showed a slight upward trend in the $P/P_0 > 0.9$

area, which was macroporous adsorption according to the adsorption principle, indicating that a macroporous structure was formed. The pore size distribution in Figure 1b further demonstrates the existence of a bimodal porous structure. All catalysts showed protrusions after 60 nm, while only one sharp peak around 8 nm can be seen from 8% Ni/MA (mesoporous alumina), indicating that there were a large number of mesopores and a small number of macropores. As can be seen from Table 1, in addition to the 4% Ni/M100-MA catalyst, the specific surface area of the remaining catalysts increased as the nickel loading increased. Although nickel particles occupy the surface of the catalyst, they also provide the surface area. For 8% Ni/MA and 8% Ni/M100-MA, the BET (initials of Brunauer, Emmett and Teller) surface areas of 8 %Ni/MA and 8% Ni/M100-MA were 109.4 and 110.1 m²/g, respectively, and the pore volume was decreased from 0.24 to 0.18 cm³/g.

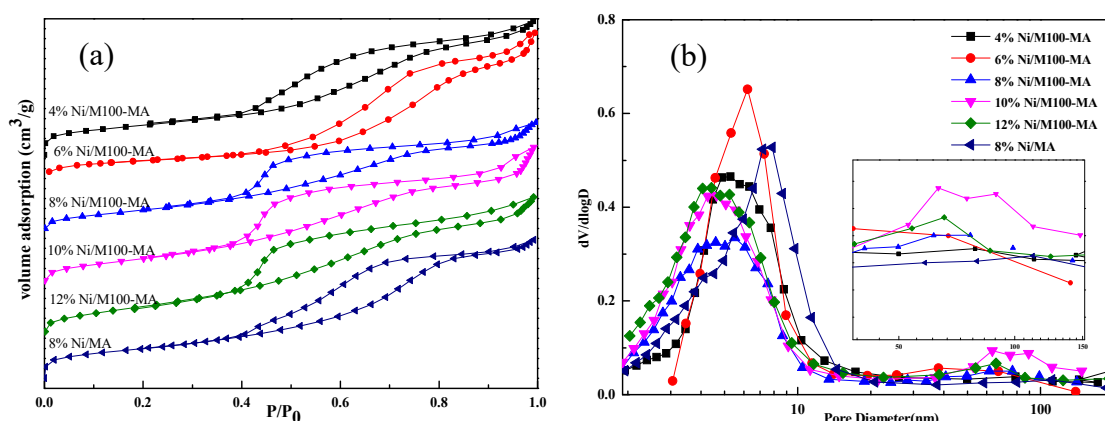


Figure 1. N₂ adsorption–desorption isotherms (a) and pore size distribution (b).

Table 1. Surface area and pore parameters of the samples.

Sample	BET Surface (m ² /g)	Pore Volume (cm ³ /g)	Pore Diameter (nm)
4% Ni/M100-MA	109.4	0.21	5.3
6% Ni/M100-MA	106.5	0.23	6.2
8% Ni/M100-MA	110.1	0.18	5.5
10% Ni/M100-MA	128.5	0.23	4.6
12% Ni/M100-MA	142.5	0.23	4.4
8% Ni/MA	109.4	0.24	7.8

Figure 2a,b show the wide-angle and low-angle XRD spectra of the samples after calcination. It can be clearly seen from Figure 2a that there are diffraction peaks appearing at $2\theta = 37.0^\circ$, 45.3° , and 66.4° . According to the PDF (10-0339) card, the diffraction peaks are attributed to NiAl₂O₄, which indicates that nickel species combine with alumina to form a new crystalline phase at high temperature. All samples have no obvious diffraction peaks of nickel species and alumina. The low-angle XRD spectrum is shown in Figure 2b. Diffraction peaks appear near $2\theta = 1^\circ$, which are attributed to the (110) crystal plane of γ -Al₂O₃, indicating the presence of ordered mesopores in the sample. It is stated that a series of catalysts prepared have a large number of highly ordered mesoporous structures. The calcined samples were reduced by flowing 10% H₂/Ar at 900 °C and new diffraction peaks can be clearly observed in the reduced XRD spectrum (Figure 2c), which are attributed to the (111), (200), and (220) crystal planes (44.5° , 51.8° , and 76.4°) of Ni and the (311), (222), (400), and (440) crystal planes (37.6° , 39.5° , 45.7° , and 66.6°) of Al₂O₃ according to the PDF (04-0850) and (29-0063) card. It can be calculated that the nickel particle size of 8%Ni/MA and 8%Ni/M100-MA is 6.5 and 5.5 nm, respectively. The nickel particle of 8%Ni/M100-MA is smaller than that of 8%Ni/MA.

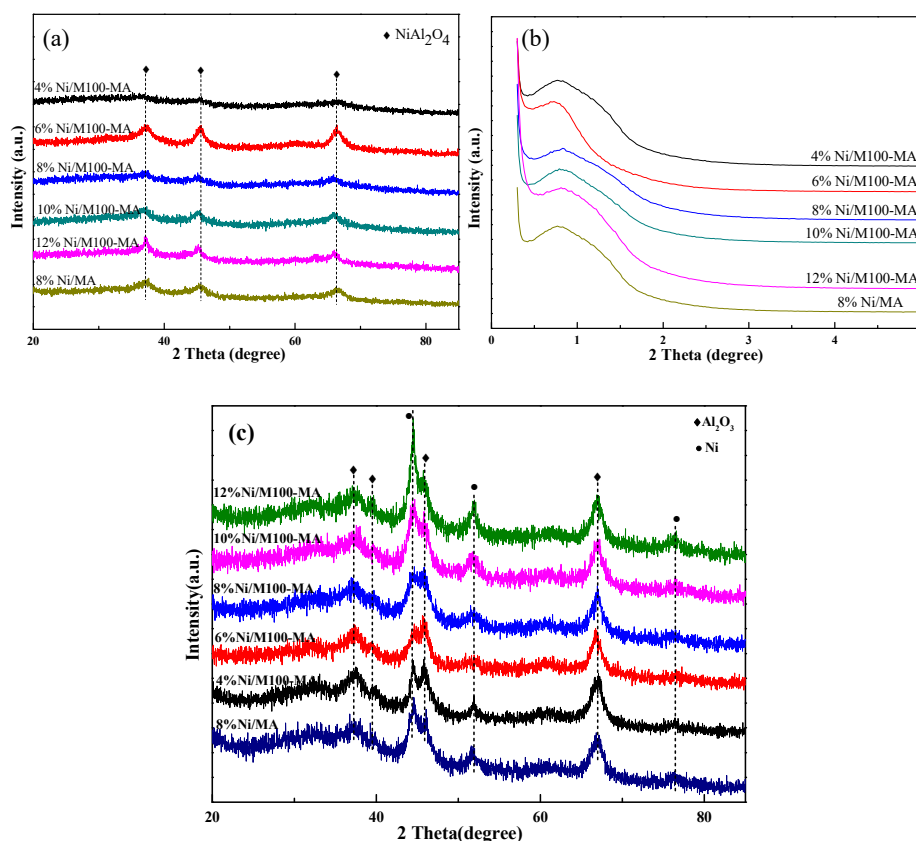


Figure 2. Wide-angle XRD patterns (a) and low-angle XRD patterns (b) of the calcined samples; (c) wide-angle XRD patterns of the reduced samples.

H₂-TPR is obtained to further understand the interaction between the metal and support of the catalyst. Figure 3 shows the H₂-TPR curve of the sample after calcination. As can be seen, all catalysts have reduction peaks at high temperature. This is attributed to the reduction of Ni²⁺ to Ni⁰ in NiAl₂O₄, indicating that there is a strong metal–support interaction in the catalyst. With the increase in nickel loading, the reduction temperature increases gradually, and the area of the reduction peak also increases gradually, which contributes to the greater amount of NiAl₂O₄ formed. The relative H₂ consumption amounts based on the 4%Ni/M100-MA of 4%Ni/M100-MA, 6%Ni/M100-MA, 8%Ni/M100-MA, 10%Ni/M100-MA, and 12%Ni/M100-MA are 1.00, 1.48, 1.83, 2.43, and 2.74, respectively, which means the amount of H₂ consumption monotone increases with the nickel loading. The H₂ consumption of 8%Ni/M100-MA is slightly lower than twice as much as that of 4%Ni/M100-MA, and the same regularity as 6%Ni/M100-MA and 12%Ni/M100-MA, indicating that the metal oxide in the samples was not completely reduced as the nickel loading increased. Compared to 759 °C of 8%Ni/MA, it is the macropores that preserved the weak interaction with metal Ni particles, resulting in a low reduction temperature [28]. The coexistence of low- and high-temperature peaks in 8%Ni/MA indicates the coexistence of a weak interaction and strong interaction.

The surface morphology of samples is displayed in Figure 4. It is clear that abundant macropores and mesopores are formed in M100-MA (in Figure 4a), indicating that the bimodal porous structure of the support was successfully prepared, and the structure was not damaged after impregnating the nickel content (in Figure 4). This result is in good agreement with that of the pore size distribution. Figure 5 shows the transmission electron microscope (TEM) images of 4%, 6%, 8%, 10%, and 12%Ni/M100-MA samples unreduced, respectively. Nickel-based particles in the samples can be faintly observed in Figure 5 that correspond to the dark spots [29]. There is no obvious metal agglomeration on the catalyst surface and Ni-based particles dispersed uniformly. No metal particles

detached from the surface of the support were observed, which indirectly indicated that a strong interaction between the metal and support was formed, consistent with the H₂-TPR results.

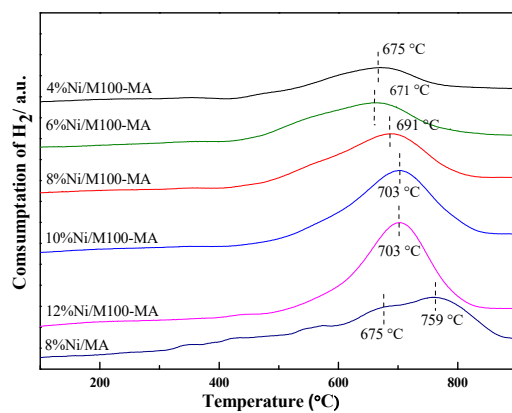


Figure 3. H₂-TPR profiles of the samples.

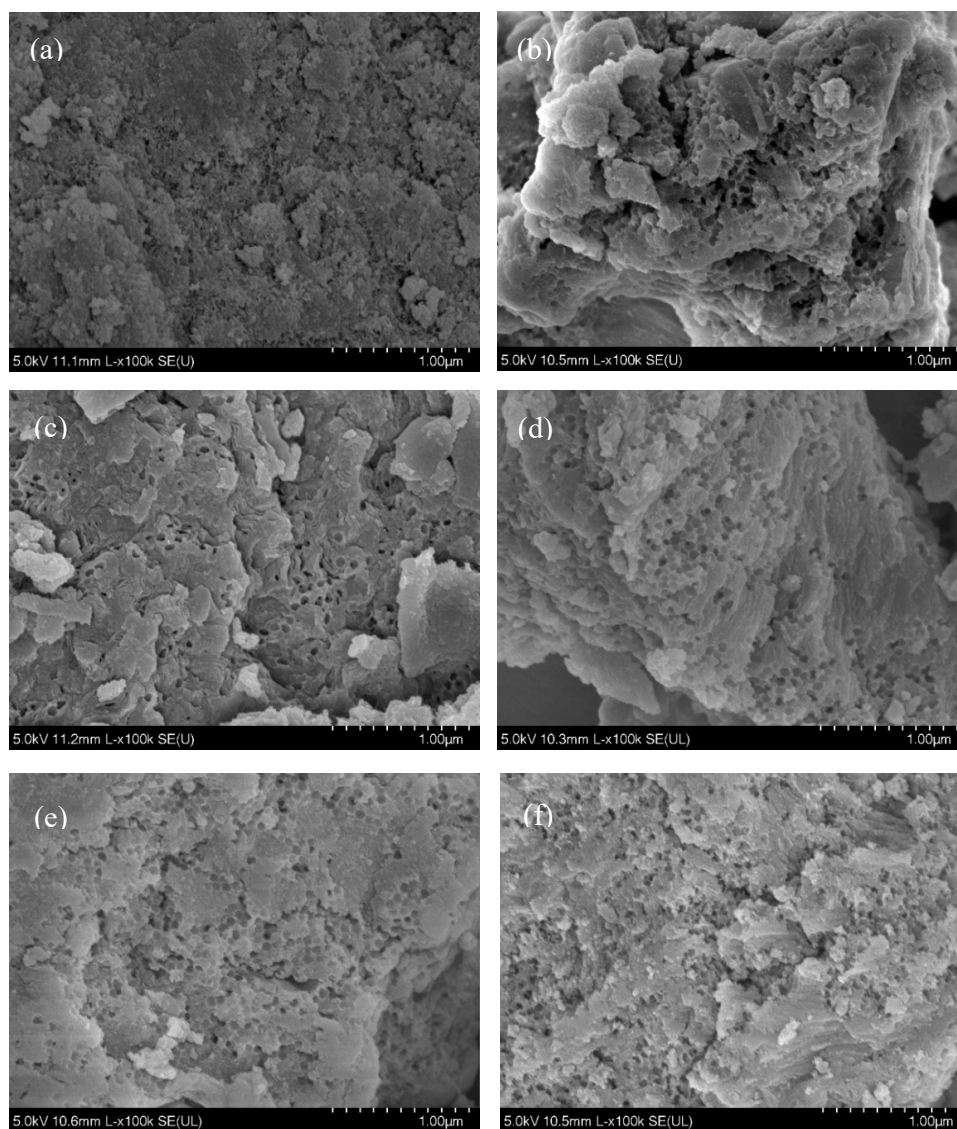


Figure 4. Scanning electron microscope (SEM) images of M100-MA (a), 4%Ni/M100-MA (b), 6%Ni/M100-MA (c), 8% Ni/M100-MA (d), 10% Ni/M100-MA (e), and 12% Ni/M100-MA (f).

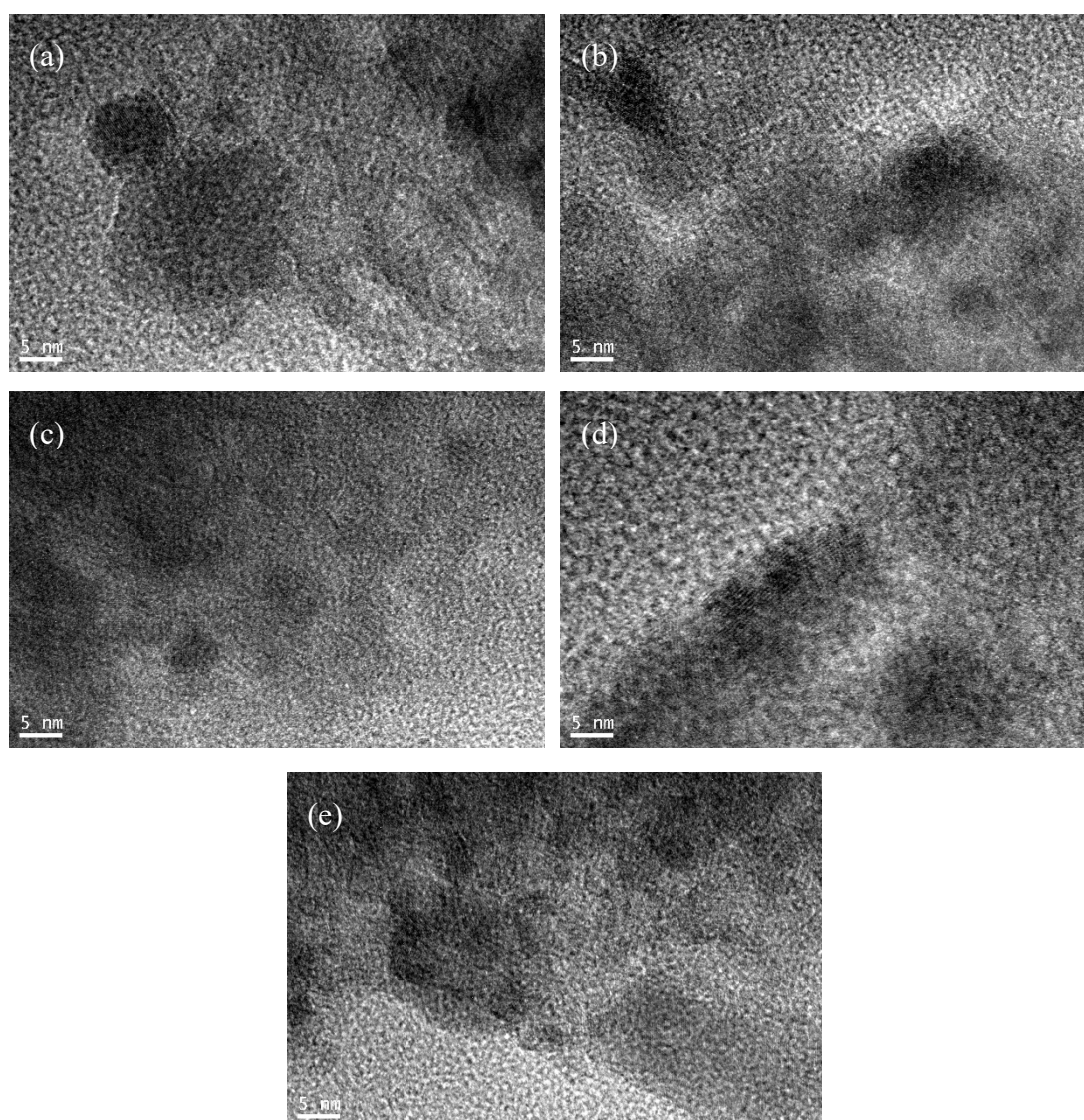


Figure 5. TEM images of 4% Ni/M100-MA (a), 6% Ni/M100-MA (b), 8% Ni/M100-MA (c), 10% Ni/M100-MA (d), and 12% Ni/M100-MA (e).

The TEM images of the reduced catalysts (Figure 6) clearly show the nickel particles and mesoporous alumina channels, confirming the construction of ordered mesoporous structured catalysts. It can be observed that there are Ni particles positioned inside the pore channels, evidencing that all the Ni particles were successfully confined by the support [30]. The average sizes of Ni particles were around 5–8 nm and the mean diameters of mesoporous alumina were about 6.6 nm which were consistent with the pore diameter shown in Table 1.

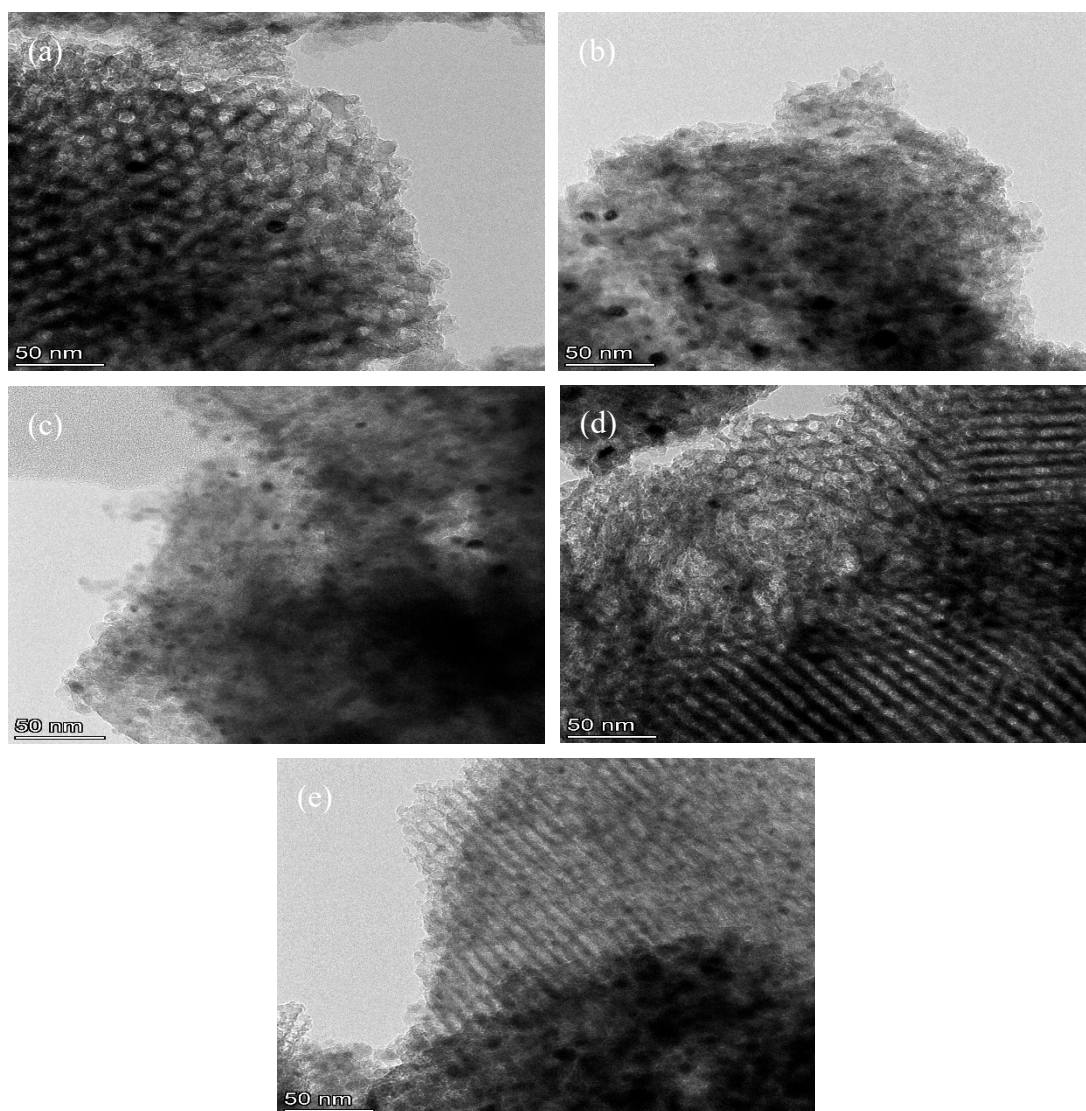


Figure 6. TEM images of reduced catalysts. 4 % Ni/M100-MA (a), 6 % Ni/M100-MA (b), 8 % Ni/M100-MA (c), 10 % Ni/M100-MA (d), and 12 % Ni/M100-MA (e).

2.2. Catalytic Performance Test

To further determine the optimum nickel loading, all catalysts were evaluated for 100 h, and the results are shown in Figure 7. It can be seen that 4% Ni/M100-MA showed poor activity. After several hours of reaction, the conversion rate decreased drastically and there was obvious deactivation, indicating that the catalyst was poor both in stability and activity. The 12% Ni/M100-MA catalyst showed the best activity and stability. The conversion rate after 100 h was higher than that of other catalysts. The conversion of CH₄ and CO₂ reached 75.0% and 84.0%, respectively, which was higher than that of other previous studies (Table 2). The catalyst has a high nickel loading, a large specific surface area, and a strong interaction between the metal and the support, so that it has the best catalytic activity. It can be seen from Table 2 that as the nickel loading increases, the initial activity of catalysts becomes higher and higher, proportional to the nickel loading, and the loadings of 6%, 8%, and 10% were similar in conversion rate after 100 h of reaction, while the equilibrium conversion of CH₄ and CO₂ of the DRM reaction at 700 °C was 99.9% and 99.9%, respectively (according to Aspen simulation results and considering side effects). Meanwhile, only CO and H₂ were detected by on-line GC analysis, showing the absolute selectivity to target products (>99%) [31].

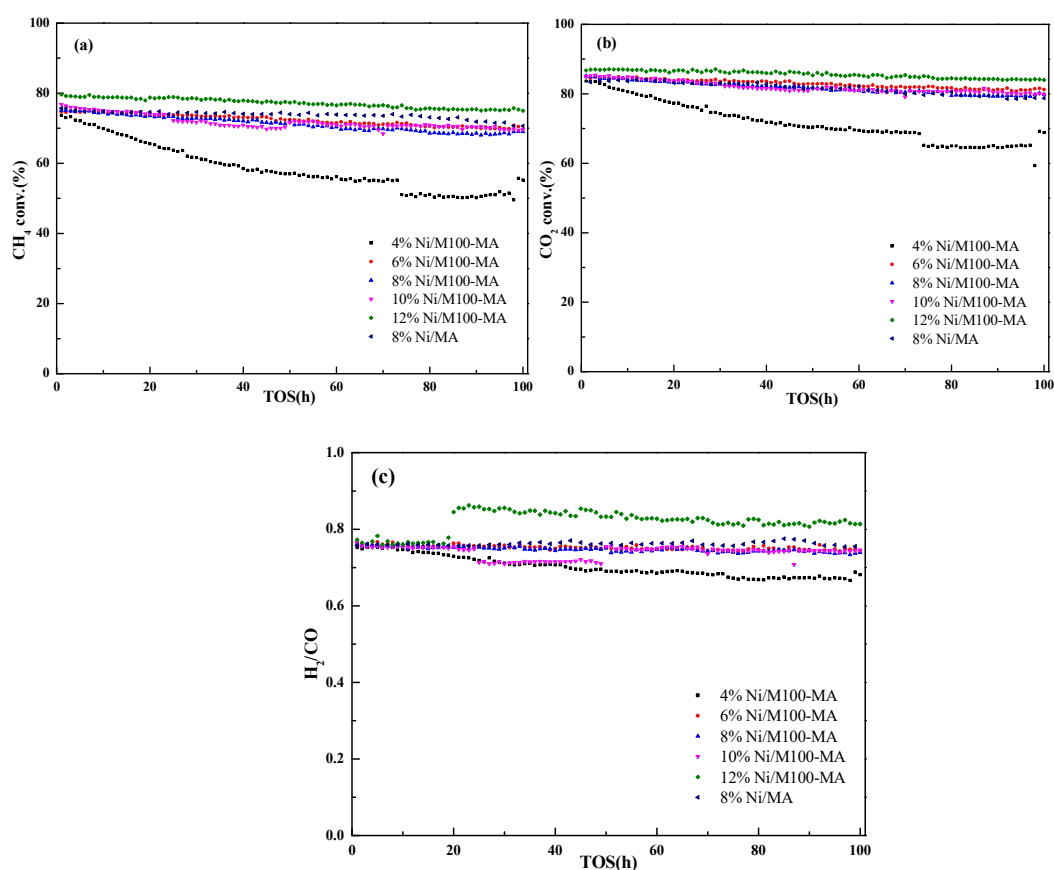


Figure 7. Evaluation of CH₄ conversion (a), CO₂ conversion (b), and H₂/CO (c) over catalysts during the dry reforming of methane (DRM) reaction. Reaction conditions: CH₄/CO₂/Ar = 45/45/10, W/F = 1 g·h/mol, T = 700 °C, TOS = 100 h.

Wang et al. [32] studied the Ni/ γ -Al₂O₃ catalysts prepared using atomic layer deposition (ALD) as well as impregnation methods to investigate the moderate Ni loading. The results showed that the Ni loading has a vital impact on the catalytic performance and the best catalytic performance is shown in Table 2. Shen et al. [33] designed the Ni-based catalysts supported on nanosheet (S), nanofiber (F), and particle (P) alumina, and the Ni/Al₂O₃-F catalyst achieved the highest stability with no sign of deactivation. Zhang's team [34] investigated a series of Ni/MgO-Al₂O₃ catalysts prepared by a simple two-step hydrothermal method and the better catalytic activity is displayed in Table 2.

Table 2. Comparison with previous literature.

Catalyst	Temperature (°C)	Cat.Weight (g)	^a TOS (h)	Conv. (%)		Ref.
				CH ₄	CO ₂	
Ni _{1.6} / γ -Al ₂ O ₃	700	0.1	35	55.8	64.3	[32]
Ni/Al ₂ O ₃ -F	750	0.2	10	80	82.5	[33]
Ni/MgO-Al ₂ O ₃ (15%)	650	0.1	10	52	64	[34]
12%Ni-M100-MA	700	0.1	100	75.0	84.0	This work

^a TOS means time on stream.

2.3. Spent Catalysts Characterization

In order to study the phase composition of spent catalysts with different Ni loadings after the reaction, the catalysts after reaction were characterized by XRD. The results are shown in Figure 8. All samples still showed the (111) and (200) crystal planes of Ni (44.5°, 51.8°), indicating that the metal Ni was not completely oxidized during the reaction. They also showed the (311), (400), and (440)

crystal planes of Al_2O_3 (37.5° , 45.7° , and 66.6°). As is apparent from Figure 8, the intensity of the nickel diffraction peak increases as the nickel loading increases. The 8% Ni/M100-MA, 10% Ni/M100-MA, and 12% Ni/M100-MA catalysts show diffraction peaks of graphite carbon at $2\theta = 26.3^\circ$, and the diffraction peaks intensity increases as the nickel loading increases, and this indicates that the catalyst with a large nickel loading tends to produce graphitic carbon [35] after the reaction. Further, the intensity of the graphite carbon diffraction peaks of 8%Ni/MA is higher than that of 8%Ni/M100-MA, indicating the 8%Ni/M100-MA is more conducive to anti-carbon.

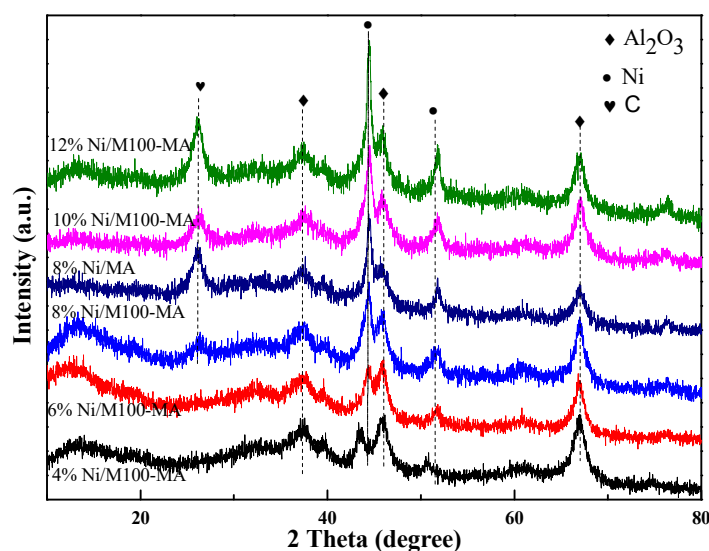


Figure 8. XRD patterns of the spent catalysts.

In order to analyze the carbon deposition behavior of the catalysts, the catalysts after the reaction were characterized by TG in an air atmosphere to quantitatively detect the carbon content. As shown in Figure 9, different nickel loadings catalysts exhibited varying degrees of carbon deposition. As the nickel loading increases, the weight loss of carbon increases gradually, which indicates that the carbon deposition of the catalyst increases with the increase in nickel loading, which is consistent with the XRD characterization. From the TG curves, the main exothermic peak at $450\text{--}700^\circ\text{C}$ was due to the removal of the inert carbon which destroyed the active sites and deactivated catalysts. The amounts of the inert carbon on spent 8%Ni/MA and 8%Ni/M100-MA were quantitatively estimated to be 18.0% and 8.2%. TG results strongly suggest that 8%Ni/M100-MA has better coke resistance during the DRM reaction.

Many efforts have been reported to lower the carbon deposition. Some of them improved the synthesis method of the catalyst: Fang et al. [36] prepared the 12%Ni- Al_2O_3 catalyst by the evaporation-induced self-assembly method (EISA). After a 20-h stability test, the weight loss of 12%Ni- Al_2O_3 -EISA was 28%, much lower than that of 12%Ni- Al_2O_3 -IMP (impregnation method) which was 64%. Huang and his coworkers [37] reported that the 12%Ni@ Al_2O_3 catalyst prepared by the inverse micro-emulsion technique performed with higher catalytic activity and better carbon deposition resistance than that of 12%Ni/ Al_2O_3 (prepared by the impregnation method). The amount of carbon decreased to 15% compared with 54% of 12%Ni/ Al_2O_3 .

To further reveal the deposited carbon, the TEM images of spent catalysts after 100 h of reaction are displayed in Figure 10. It can be seen that the catalyst has a large number of carbon nanotubes generated. The formation of carbon nanotubes could weaken the interaction between the metallic Ni and support, making Ni particles separate from the mesoporous pores and migrate to the surface of the support, resulting in Ni particle agglomeration. There is a serious agglomeration of Ni particles in the 12%Ni/M100-MA catalyst (in Figure 10d), but it maintained good dispersion on the 6%Ni/M100-MA catalyst (in Figure 10a), which was attributed to the catalyst with a small Ni particle size and the strong metal–support interaction had stronger anti-carbon deposition performance [27].

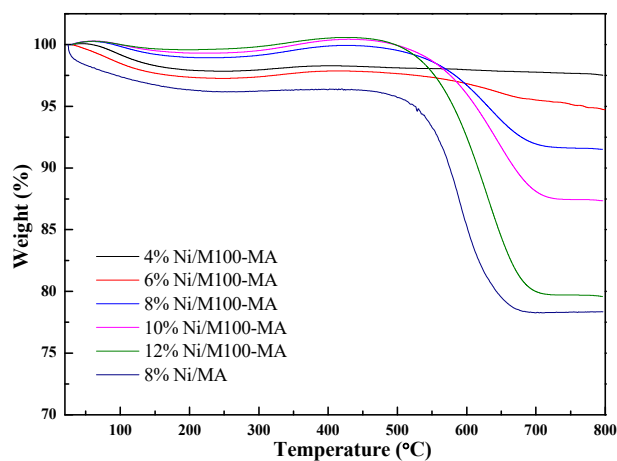


Figure 9. TG profiles of the spent catalysts.

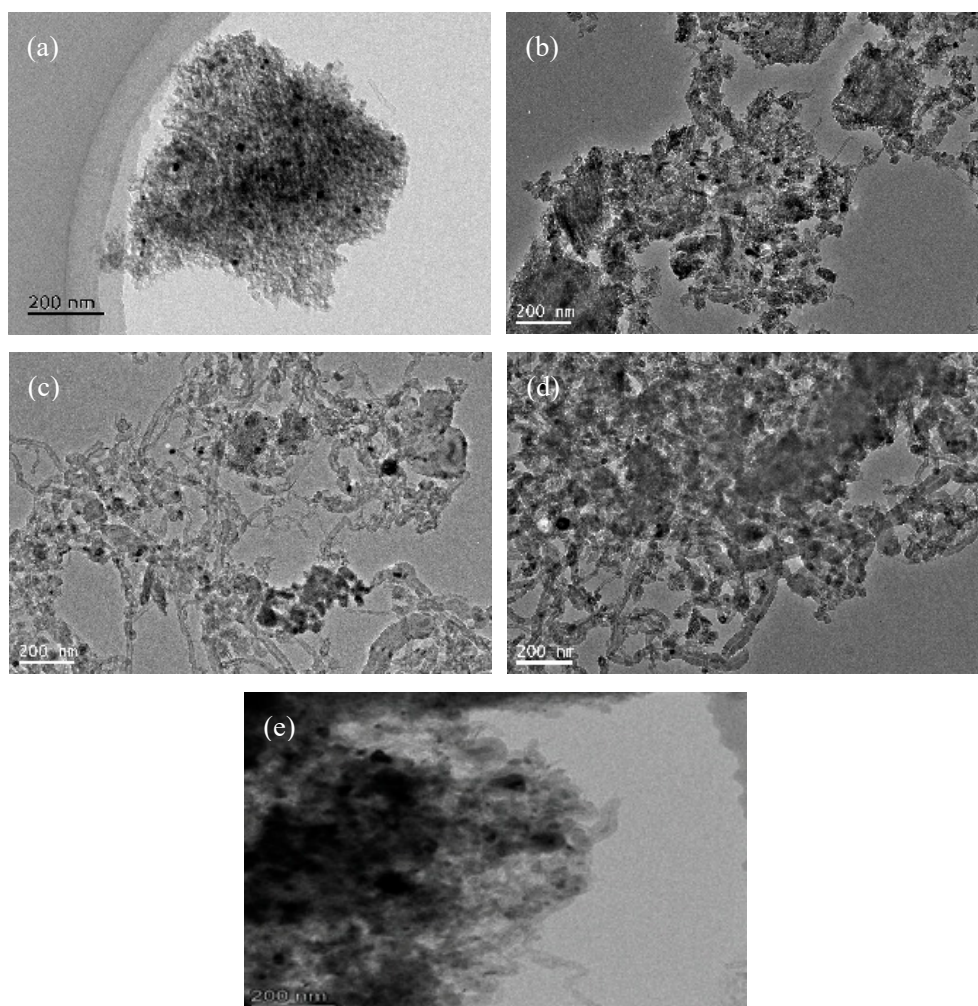


Figure 10. TEM images of spent catalysts. 4% Ni/M100-MA (a), 6% Ni/M100-MA (b), 8% Ni/M100-MA (c), 10% Ni/M100-MA (d), and 12% Ni/M100-MA (e).

TPH was attained to further determine the type of carbon deposition of the catalyst after the reaction. As shown in Figure 11, the main hydrogen-consuming peaks of the catalyst appear around 600 °C because of the hydrogenation of carbon nanotubes. As the nickel loading increases, the peak intensity and peak area are also constantly increasing, which indicates that the amount of carbon

nanotubes is also increasing. It can be seen that the amount of carbon deposition increases with the increase in nickel loading, especially the number of carbon nanotubes, which is consistent with the result of the TG and XRD characterization. It can be also observed that there is more graphite carbon formed on the spent 8%Ni/MA than that on the spent 8%Ni/M100-MA.

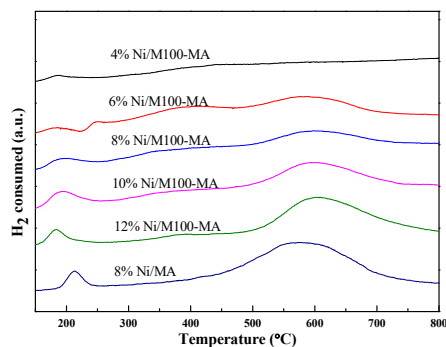


Figure 11. TPH profiles of the spent catalysts.

The type of carbon species on the surface of catalysts can also be analyzed by Raman spectroscopy. Catalysts were measured with a 780 nm excitation source at a Raman shift of 1000 cm^{-1} – 1800 cm^{-1} , as shown in Figure 12. The catalysts still have characteristic peaks: D peaks and G peaks, of carbon materials around 1300 cm^{-1} and 1580 cm^{-1} . The larger I_D/I_G indicates the greater disorder of carbon materials. By calculation, the R ($R = I_D/I_G$) values of the 4% Ni/M100-MA, 6% Ni/M100-MA, 8% Ni/M100-MA, 8% Ni/MA, 10% Ni/M100-MA, and 12% Ni/M100-MA catalysts were, respectively, 1.23, 1.23, 1.09, 0.75, 1.01, and 0.98, and it can be seen that as the nickel loading increases, the degree of graphitization of the formed carbon is gradually deepened, which is consistent with the TPH characterization results. Further, the carbon deposition species on the spent 8%Ni/MA exhibited a higher graphite degree than that on the spent 8%Ni/M100-MA.

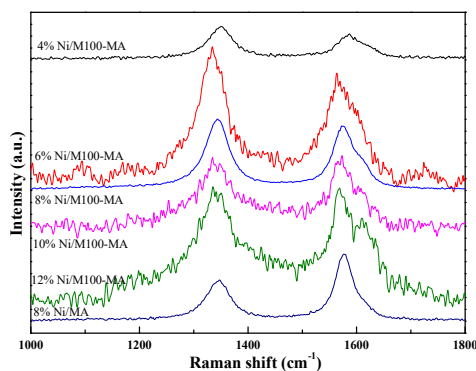


Figure 12. Raman spectra of the spent catalysts.

3. Experimental Section

3.1. Catalyst Preparation and Characterization

Given amounts of templating agent P123, aluminum isopropoxide, and concentrated nitric acid were dissolved in absolute ethanol while stirring vigorously for 5 h. Then, an appropriate amount of polystyrene (PS) pellet (100 nm) was added to the above solution and stirring was continued for 5 min (mesoporous support was no PS pellet). The mixed solution was dried at $60\text{ }^\circ\text{C}$ for 72 h, then the dried sample was calcined at $700\text{ }^\circ\text{C}$ for 4 h in air atmosphere to obtain a bimodal porous structure support, which was named M100-MA. Then, it was impregnated on the M100-MA with a given amount of nickel nitrate, dried at $120\text{ }^\circ\text{C}$ for 12 h, and calcined at $700\text{ }^\circ\text{C}$ for 4 h in air atmosphere to obtain a

bimodal porous structure catalyst, which was recorded as Ni/M100-MA [38]. Nickel loadings in this paper are mass percentages.

Powder X-ray diffractograms (XRD) of the catalysts were recorded by using Bruker's D8 Advance X-ray diffractometer (Karlsruhe, Germany) (CuK α radiation) in the 3°–85° range (2°/min, 0.02° increment).

The N₂ physical adsorption–desorption was analyzed by the JW-BK122F specific surface and aperture analyzer (Jingwei Gaobo, Beijing, China). Prior to testing, the sample was degassed under vacuum at 200 °C for 2 h to remove moisture and adsorbed impurities. The N₂ adsorption–desorption isotherm was measured at 77 K. The specific surface area of the catalyst was calculated according to the BET equation, and the pore size distribution was calculated by the BJH (initials of Barrett, Joyner and Halenda) method.

H₂ temperature programmed reduction (H₂-TPR) was tested by the AutoChem II2920 automatic temperature programmed chemical adsorption instrument from Micromeritics, Norcross, GA, USA. The test conditions were as follows: The sample (50 mg) was heated up to 350 °C at a rate of 10 °C/min, and purged in 30 mL/min flowing helium for 1 h, reduced to 50 °C, and purged with 10% H₂/Ar at a gas flow rate of 30 mL/min until the baseline was stable, then heated up to 900 °C at a rate of 10 °C/min, and the reduction curve was recorded simultaneously.

The transmission electron microscope (TEM) was tested with the Japanese JEM-2100F transmission electron microscope (Shojima, Tokyo, Japan), and the accelerating voltage was 200 kV. The scanning electron microscope (SEM) was tested with the Zeiss SUPRA55 scanning electron microscope (Jena, Germany), and the accelerating voltage was 3 kV.

Temperature programmed hydrogenation (TPH) was tested by the AutoChem II2920 automatic temperature programmed chemical adsorption instrument from Micromeritics, Norcross, GA, USA. The test conditions were as follows: A 40 mg spent catalyst was raised to the temperature of 150 °C at a rate of 10 °C/min, and purged with helium at a gas flow rate of 30 mL/min for 1 h, lowered to 50 °C, and switched to 10% H₂/Ar, purged at a gas flow rate of 30 mL/min until the baseline was stable, then warmed up to 900 °C at a rate of 10 °C/min, and the reduction curve was recorded simultaneously.

Laser Raman spectroscopy (Raman) was carried out by HIRR high-resolution micro-Raman spectroscopy from Horiba, Paris, France. We preheated the Raman spectroscopy for 30 min before testing. The grinded sample was tested at 780 nm.

The carbon deposition resistance of catalysts was investigated by using thermogravimetric analysis (TG) (SETSYS16 comprehensive thermal analyzer, Setaram, Lyons, France). Catalysts were heated from room temperature to 800 °C in an air atmosphere at a heating rate of 10 °C/min.

3.2. Catalytic Test

Catalytic measurement was performed in a fixed bed reactor. The quartz reaction tube with an inner diameter of 6 mm was used as the reactor, and quartz sand (0.3 g) was to the catalyst (0.1 g) in reactor. The catalyst was uniformly mixed with quartz sand and charged into the middle of the quartz reaction tube, and then the quartz wool was filled in the front and rear positions of the catalyst for fixation. After that, we purged it with argon at a flow rate of 40 mL/min and checked the air tightness with soapy water. After that, we raised the temperature to the reduction temperature in argon atmosphere, then reduced the catalyst in a 40 mL/min flowing reducing gas (5% H₂/95% N₂). After reduction, we switched to the feed gas (CH₄/CO₂/Ar) for the reaction, and the reaction tail gas was detected on-line using GC-9560 chromatography (Shanghai, China) after removing water by cold trap condensation.

The reaction conditions were as follows: 0.1 g of catalyst (20–40 mesh), reduced at 700 °C for 2 h, CH₄/CO₂/Ar = 45/45/10, W/F = 1 g·h/mol, and the reaction temperature was 700 °C.

3.3. Results Calculation

During the experiment, Ar is used as the internal standard gas and does not participate in the reaction. The conversion rate can be calculated by the content of Ar in the tail gas. The calculation formula is as follows:

Conversion rate of CO₂:

$$\text{Conv.CO}_2(\%) = \frac{A_{\text{CO}_2}^{\text{in}}/A_{\text{Ar}}^{\text{in}} - A_{\text{CO}_2}^{\text{out}}/A_{\text{Ar}}^{\text{out}}}{A_{\text{CO}_2}^{\text{in}}/A_{\text{Ar}}^{\text{in}}} \times 100\%$$

Conversion rate of CH₄:

$$\text{Conv.CH}_4(\%) = \frac{A_{\text{CH}_4}^{\text{in}}/A_{\text{Ar}}^{\text{in}} - A_{\text{CH}_4}^{\text{out}}/A_{\text{Ar}}^{\text{out}}}{A_{\text{CH}_4}^{\text{in}}/A_{\text{Ar}}^{\text{in}}} \times 100\%$$

A_i represents the chromatographic peak area of component i.

4. Conclusions

In summary, a series of bimodal porous structure catalysts with different nickel loadings were prepared by the impregnation method. XRD, pore size distribution, and other characterizations indicate that the catalysts exhibit highly ordered mesoporous channels and a macroporous structure. As the nickel loading increases, the specific surface area of catalysts gradually increases, the interaction between the metal and support gradually increases, and the catalytic activity is also continuously enhanced. The carbon deposition amount and graphitization degree of catalysts increase with the increase in nickel loading, so that the carbon deposition resistance of catalysts gradually decreases. As the nickel loading doubled, the catalytic activity of the catalyst did not improve significantly, while the amount of carbon deposits increased a lot. Raman characterization showed that the catalyst with a lower Ni content has a lower degree of graphitization of carbon deposits formed after the DRM reaction, and the generated amorphous carbon is easily eliminated by CO₂. Therefore, the more optimal nickel loadings are 6% and 8%, as the CH₄ and CO₂ conversion rates reached 69.7%, 81.2% and 69.1%, 79.8% after 100 h of reaction, respectively; the carbon content is just 5.3% and 8.3%, respectively, lower than that of the spent 8%Ni/MA (21.6%). The application of the bimodal porous structure in Ni-based catalysts was successful [37] and provided a promising result for highly active as well as stable Ni/Al₂O₃ catalysts for the DRM reaction.

Author Contributions: Conceptualization, Q.M. and J.S.; methodology, L.L. and Y.H.; formal analysis, S.M., X.G., J.Z. and H.F.; investigation, T.Z.; writing—original draft preparation, L.L. and Y.H.; writing—review and editing, Q.M., J.S. and T.-S.Z. All authors have read and agreed to the published version of the manuscript.

Funding: This research received no external funding.

Acknowledgments: The authors thank the financial support from National Natural Science Foundation of China (21766027), Ningxia Natural Science Foundation (2020AAC03023), the East-West Cooperation Project of Ningxia Key R & D Plan (2017BY063), Western youth scholar Talents Project of CAS (Grant No. XAB2016AW03) and the Foundation of State Key Laboratory of High-efficiency Coal Utilization and Green Chemical Engineering (Grant No. 2019-KF-11).

Conflicts of Interest: The authors declare no conflict of interest.

References

1. Yide, X.U.; Bao, X.; Lin, L. Direct conversion of methane under nonoxidative conditions. *J. Catal.* **2003**, *216*, 386–395.
2. Lin, Q.; Zhang, Q.; Yang, G.; Chen, Q.; Li, J.; Wei, Q.; Tan, Y.; Wan, H.; Tsubaki, N. Insights into the promotional roles of palladium in structure and performance of cobalt-based zeolite capsule catalyst for direct synthesis of C₅–C₁₁ iso-paraffins from syngas. *J. Catal.* **2016**, *344*, 378–388. [[CrossRef](#)]

3. Behrens, M.; Studt, F.; Kasatkin, I.; Kühl, S.; Hävecker, M.; Abild-Pedersen, F.; Zander, S.; Girgsdies, F.; Kurr, P.; Knief, B.L.; et al. The active site of methanol synthesis over Cu/ZnO/Al₂O₃ industrial catalysts. *Science* **2012**, *336*, 893–897. [[CrossRef](#)]
4. Wysocka, I.; Hupka, J.; Rogala, A. Catalytic Activity of Nickel and Ruthenium-Nickel Catalysts Supported on SiO₂, ZrO₂, Al₂O₃, and MgAl₂O₄ in a Dry Reforming Process. *Catalysts* **2019**, *9*, 540. [[CrossRef](#)]
5. Lu, Y.; Jiang, S.; Wang, S.; Zhao, Y.; Ma, X. Effect of the addition of Ce and Zr over a flower-like NiO-MgO (111) solid solution for CO₂ reforming of methane. *J. CO₂ Util.* **2018**, *26*, 123–132. [[CrossRef](#)]
6. Kim, A.R.; Lee, H.Y.; Cho, J.M.; Choi, J.H.; Bae, J.W. Ni/M-Al₂O₃ (M = Sm, Ce or Mg) for combined steam and CO₂ reforming of CH₄ from coke oven gas. *J. CO₂ Util.* **2017**, *21*, 211–218. [[CrossRef](#)]
7. Wei, Q.; Yang, G.; Gao, X.; Yamane, N.; Zhang, P.; Liu, G.; Tsubaki, N. Ni/Silicalite-1 coating being coated on SiC foam: A tailor-made monolith catalyst for syngas production using a combined methane reforming process. *Chem. Eng. J.* **2017**, *327*, 465–473. [[CrossRef](#)]
8. Kawi, S.; Kathiraser, Y.; Ni, J.; Oemar, U.; Li, Z.; Saw, E.T. Progress in Synthesis of Highly Active and Stable Nickel-Based Catalysts for Carbon Dioxide Reforming of Methane. *ChemSusChem* **2015**, *8*, 3556–3575. [[CrossRef](#)]
9. Li, H.; Wang, J. Study on CO₂ reforming of methane to syngas over Al₂O₃-ZrO₂ supported Ni catalysts prepared via a direct sol-gel process. *Chem. Eng. Sci.* **2004**, *59*, 4861–4867. [[CrossRef](#)]
10. Carvalho, D.C.; de Souza, H.S.; Josué Filho, M.; Oliveira, A.C.; Campos, A.; Milet, É.R.; de Sousa, F.F.; Padron-Hernandez, E.; Oliveira, A.C. A study on the modification of mesoporous mixed oxides supports for dry reforming of methane by Pt or Ru. *Appl. Catal. B Environ.* **2014**, *473*, 132–145. [[CrossRef](#)]
11. Köpfle, N.; Götsch, T.; Grünbacher, M.; Carbonio, E.A.; Hävecker, M.; Knop-Gericke, A.; Schlicker, L.; Doran, A.; Kober, D.; Gurlo, A.; et al. Zirconium-assisted activation of palladium to boost syngas production by methane dry reforming. *Angew. Chem. Int. Ed.* **2018**, *57*, 14613–14618. [[CrossRef](#)] [[PubMed](#)]
12. Yentekakis, I.V.; Goula, G.; Hatzisymeon, M.; Betsi-Argyropoulou, I.; Botzoulaki, G.; Kousi, K.; Kondarides, D.I.; Taylor, M.J.; Parlett, C.M.; Osatiashtiani, A.; et al. Effect of support oxygen storage capacity on the catalytic performance of Rh nanoparticles for CO₂ reforming of methane. *Appl. Catal. B Environ.* **2019**, *243*, 490–501. [[CrossRef](#)]
13. Das, S.; Shah, M.; Gupta, R.K.; Bordoloi, A. Enhanced dry methane reforming over Ru decorated mesoporous silica and its kinetic study. *J. CO₂ Util.* **2019**, *29*, 240–253. [[CrossRef](#)]
14. Richardson, J.T.; Paripatyadar, S.A. Carbon dioxide reforming of methane with supported rhodium. *Appl. Catal.* **1990**, *61*, 293–309. [[CrossRef](#)]
15. Boukha, Z.; Kacimi, M.; Pereira, M.F.; Faria, J.L.; Figueiredo, J.L.; Ziyad, M. Methane dry reforming on Ni loaded hydroxyapatite and fluoroapatite. *Appl. Catal. A Gen.* **2007**, *317*, 299–309. [[CrossRef](#)]
16. Wu, Z.; Yang, B.; Miao, S.; Liu, W.; Xie, J.; Lee, S.; Pellin, M.J.; Xiao, D.; Su, D.; Ma, D. Lattice strained Ni-Co alloy as a high-performance catalyst for catalytic dry reforming of methane. *ACS Catal.* **2019**, *9*, 2693–2700. [[CrossRef](#)]
17. Yan, X.; Hu, T.; Liu, P.; Li, S.; Zhao, B.; Zhang, Q.; Jiao, W.; Chen, S.; Wang, P.; Lu, J.; et al. Highly efficient and stable Ni/CeO₂-SiO₂ catalyst for dry reforming of methane: Effect of interfacial structure of Ni/CeO₂ on SiO₂. *Appl. Catal. B Environ.* **2019**, *246*, 221–231. [[CrossRef](#)]
18. Kalai, D.Y.; Stangeland, K.; Jin, Y.; Tucho, W.M.; Yu, Z. Biogas dry reforming for syngas production on La promoted hydrotalcite-derived Ni catalysts. *Int. J. Hydrog. Energy* **2018**, *43*, 19438–19450. [[CrossRef](#)]
19. Hou, Z.; Chen, P.; Fang, H.; Zheng, X.; Yashima, T. Production of synthesis gas via methane reforming with CO on noble metals and small amount of noble-(Rh-) promoted Ni catalysts. *Int. J. Hydrog. Energy* **2006**, *31*, 555–561. [[CrossRef](#)]
20. Feng, X.; Liu, J.; Zhang, P.; Zhang, Q.; Xu, L.; Zhao, L.; Song, X.; Gao, L. Highly coke resistant Mg-Ni/Al₂O₃ catalyst prepared via a novel magnesiothermic reduction for methane reforming catalysis with CO₂: The unique role of Al-Ni intermetallics. *Nanoscale* **2019**, *11*, 1262–1272. [[CrossRef](#)]
21. Movasati, A.; Alavi, S.M.; Mazloom, G. Dry reforming of methane over CeO₂-ZnAl₂O₄ supported Ni and Ni-Co nano-catalysts. *Fuel* **2019**, *236*, 1254–1262. [[CrossRef](#)]
22. Li, Z.; Wang, Z.; Kawi, S. Sintering and coke resistant core/yolk shell catalyst for hydrocarbon reforming. *ChemCatChem* **2019**, *11*, 202–224. [[CrossRef](#)]

23. Fan, X.; Liu, Z.; Zhu, Y.A.; Tong, G.; Zhang, J.; Engelbrekt, C.; Ulstrup, J.; Zhu, K.; Zhou, X. Tuning the composition of metastable $\text{Co}_x\text{Ni}_y\text{Mg}_{100-x-y}(\text{OH})(\text{OCH}_3)$ nanoplates for optimizing robust methane dry reforming catalyst. *J. Catal.* **2015**, *330*, 106–119. [[CrossRef](#)]
24. Zhou, H.; Zhang, T.; Sui, Z.; Zhu, Y.A.; Han, C.; Zhu, K.; Zhou, X. A single source method to generate Ru-Ni-MgO catalysts for methane dry reforming and the kinetic effect of Ru on carbon deposition and gasification. *Appl. Catal. B Environ.* **2018**, *233*, 143–159. [[CrossRef](#)]
25. Akri, M.; Zhao, S.; Li, X.; Zang, K.; Lee, A.F.; Isaacs, M.A.; Xi, W.; Gangarajula, Y.; Luo, J.; Ren, Y.; et al. Atomically dispersed nickel as coke-resistant active sites for methane dry reforming. *Nat. Commun.* **2019**, *10*, 5181. [[CrossRef](#)]
26. Wang, H.Y.; Ruckenstein, E. Carbon dioxide reforming of methane to synthesis gas over supported rhodium catalysts: The effect of support. *Appl. Catal. A Gen.* **2000**, *204*, 143–152. [[CrossRef](#)]
27. Sepehri, S.; Rezaei, M. Preparation of highly active nickel catalysts supported on mesoporous nanocrystalline $\gamma\text{-Al}_2\text{O}_3$ for methane autothermal reforming. *Chem. Eng. Technol.* **2015**, *38*, 1637–1645. [[CrossRef](#)]
28. Ma, Q.; Han, Y.; Wei, Q.; Makpal, S.; Gao, X.; Zhang, J.; Zhao, T.S. Stabilizing Ni on bimodal mesoporous-macroporous alumina with enhanced coke tolerance in dry reforming of methane to syngas. *J. CO₂ Util.* **2020**, *35*, 288–297. [[CrossRef](#)]
29. Li, B.; Luo, Y.; Li, B.; Yuan, X.; Wang, X. Catalytic performance of iron-promoted nickel-based ordered mesoporous alumina FeNiAl catalysts in dry reforming of methane. *Fuel Process. Technol.* **2019**, *193*, 348–360. [[CrossRef](#)]
30. Wang, F.; Han, B.; Zhang, L.; Xu, L.; Yu, H.; Shi, W. CO₂ reforming with methane over small-sized Ni@SiO₂ catalysts with unique features of sintering-free and low carbon. *Appl. Catal. B Environ.* **2018**, *235*, 26–35. [[CrossRef](#)]
31. Zhao, Y.; Kang, Y.; Li, H.; Li, H. CO₂ conversion to synthesis gas via DRM on the durable Al₂O₃/Ni/Al₂O₃ sandwich catalyst with high activity and stability. *Green Chem.* **2018**, *10*, 1039. [[CrossRef](#)]
32. Wang, G.; Luo, F.; Cao, K.; Zhang, Y.; Li, J.; Zhao, F.; Chen, R.; Hong, J. Effect of Ni content of Ni/ $\gamma\text{-Al}_2\text{O}_3$ catalysts prepared by atomic layer deposition method on CO₂ reforming of methane. *Energy Technol.* **2019**, *7*, 1800359. [[CrossRef](#)]
33. Shen, D.; Huo, M.; Li, L.; Lyu, S.; Wang, J.; Wang, X.; Zhang, Y.; Li, J. Effects of alumina morphology on dry reforming of methane over Ni/Al₂O₃ catalysts. *Catal. Sci. Technol.* **2020**, *10*, 510. [[CrossRef](#)]
34. Zhang, L.; Zhang, Q.; Liu, Y.; Zhang, Y. Dry reforming of methane over Ni/MgO-Al₂O₃ catalysts prepared by two-step hydrothermal method. *Appl. Surf. Sci.* **2016**, *389*, 25–33. [[CrossRef](#)]
35. Gucci, L.; Stefler, G.; Geszti, O.; Sajó, I.; Pászti, Z.; Tompos, A.; Schay, Z. Methane dry reforming with CO₂: A study on surface carbon species. *Appl. Catal. A Gen.* **2010**, *375*, 236–246. [[CrossRef](#)]
36. Fang, X.; Peng, C.; Peng, H.; Liu, W.; Xu, X.; Wang, X.; Li, C.; Zhou, W. Methane Dry Reforming over Coke-Resistant Mesoporous Ni-Al₂O₃ Catalysts Prepared by Evaporation-Induced Self-Assembly Method. *ChemCatChem* **2015**, *7*, 3753–3762. [[CrossRef](#)]
37. Huang, Q.; Fang, X.; Cheng, Q.; Li, Q.; Xu, X.; Xu, L.; Liu, W.; Gao, Z.; Zhou, W.; Wang, X. Synthesis of Highly Active and Stable Ni@Al₂O₃ Embedded Catalyst for Methane Dry Reforming: On the Confinement Effect of Al₂O₃ Shells for Ni Nanoparticles. *ChemCatChem* **2017**, *9*, 3563–3572. [[CrossRef](#)]
38. Yuan, Q.; Yin, A.X.; Luo, C.; Sun, L.D.; Zhang, Y.W.; Duan, W.T.; Liu, H.C.; Yan, C.H. Facile Synthesis for Ordered Mesoporous $\gamma\text{-Alumina}$ s with High Thermal Stability. *J. Am. Chem. Soc.* **2008**, *130*, 3465–3472. [[CrossRef](#)]

Publisher's Note: MDPI stays neutral with regard to jurisdictional claims in published maps and institutional affiliations.



© 2020 by the authors. Licensee MDPI, Basel, Switzerland. This article is an open access article distributed under the terms and conditions of the Creative Commons Attribution (CC BY) license (<http://creativecommons.org/licenses/by/4.0/>).